Research Article Vol. 31, No. 9 / 24 Apr 2023 / Optics Express 14196
Optics EXPRESS

Circular dichroism in a plasmonic array of elliptical nanoholes with square lattice

HANAN ALI,[1,*] EMILIJA PETRONIJEVIC,[2] GIOVANNI PELLEGRINI,[1] CONCITA SIBILIA,[2] AND LUCIO CLAUDIO ANDREANI[1]

[1]Department of Physics, University of Pavia, via Bassi 6, I- 27100 Pavia, Italy
[2]Department S.B.A.I., Sapienza Università di Roma., Via A. Scarpa 14, I- 00161, Rome, Italy
[*]hanan.ali01@universitadipavia.it

Abstract: Chiral properties of plasmonic metasurfaces, especially related to different absorption of left and right circularly polarized light leading to circular dichroism (CD), are a research hot topic in nanophotonics. There is often a need to understand the physical origin of CD for different chiral metasurfaces, and to get guidelines for the design of structures with optimized and robust CD. In this work, we numerically study CD at normal incidence in square arrays of elliptic nanoholes etched in thin metallic layers (Ag, Au, Al) on a glass substrate and tilted with respect to the symmetry axes. Strong CD arises in absorption spectra at the same wavelength region of extraordinary optical transmission, indicating highly resonant coupling between light and surface plasmon polaritons at the metal/glass and metal/air interfaces. We elucidate the physical origin of absorption CD by a careful comparison of optical spectra for different polarizations (linear and circular), with the aid of static and dynamic simulations of local enhancement of the electric field. Furthermore, we optimize the CD as a function of the ellipse parameters (diameters and tilt), the thickness of the metallic layer, and the lattice constant. We find that silver and gold metasurfaces are most useful for CD resonances above 600 nm, while aluminum metasurfaces are convenient for achieving strong CD resonances in the short-wavelength range of the visible regime and in the near UV. The results give a full picture of chiral optical effects at normal incidence in this simple nanohole array, and suggest interesting applications for chiral biomolecules sensing in such plasmonic geometries.

1. Introduction

Plasmonic nanohole arrays (NHA), i.e. periodic arrays of nanoholes realized in a metal film, have been of interest since 25 years as they can exhibit extraordinary transmission (EOT) of light [1,2]. Such phenomenon is associated with the resonant coupling of the electromagnetic field to surface plasmons polaritons (SPP) [3,4] at the interfaces between the metal layer and the surrounding dielectric media. The interpretation of EOT is, however, tricky as SPPs at the hole sidewalls also play a crucial role [5]. The resonant enhancement of the electromagnetic field associated with SPP excitations is at the heart of EOT and of various peculiar phenomena that occur in plasmonic metasurfaces [6,7], which are of interest for fundamental properties of light-matter interaction as well as for sensing applications.

Our focus here is on chiral effects that are induced when mirror symmetries in the plasmonic NHA are broken. Chirality is the absence of any symmetry plane [8] and is a common phenomenon that takes place in the macro-world and at the nanoscale, notably for molecular and biological systems [9,10], playing a crucial role in drug sciences [11]. Chiral structures respond in a different way to incident light with right circular polarization (RCP) or left circular polarization (LCP): this results in circular dichroism (CD) in optical properties like absorption, transmission, and luminescence, which is enhanced due to the plasmonic effect [12–19]. The local chirality of light can also be defined and controlled [20,21]. Chiral metamaterials and metasurfaces with enhanced CD have been realized with a number of structures including spirals,

#485324 https://doi.org/10.1364/OE.485324
Journal © 2023 Received 18 Jan 2023; revised 19 Feb 2023; accepted 3 Mar 2023; published 14 Apr 2023

Optics EXPRESS

gammadion, twisted layers, asymmetric dimers, etc [22–24]. Chiral metasurfaces [25,26] are not only a playground for basic studies of chirality in a controlled medium, but also a promising platform for the realization of compact chiral sensing devices with increased sensitivity [27–29].

A particularly simple way to obtain a NHA with chiral properties is to consider an array of elliptical nanoholes whose major/minor axes are tilted with respect to the symmetry axes of the lattice [30–33]. Elliptical Nanohole Arrays (ENHA) in a metal film arranged in a triangular lattice have been shown to display nearly maximal CD in absorption, upon optimization of hole diameters and tilting angle [31]. Moreover, ENHAs can be fabricated with a low-cost procedure based on self-assembling of polystyrene nanospheres followed by metal evaporation at oblique incidence and removal of the template [34]. Such a lattice displays intrinsic chirality, i.e., chiral behavior at normal incidence that follows from broken mirror symmetries in the structure. This is to be contrasted with extrinsic chirality [16,34,35], which occurs in a nonchiral lattice at oblique incidence when the orientation of the incident electromagnetic field is along a non-symmetry direction of the lattice.

Despite numerous investigations of chiral properties in ENHAs and in other plasmonic metasurfaces, the origin of circular dichroism and its relation to EOT and SPP properties have not been explored in detail until now. Furthermore, most numerical studies of CD in plasmonic NHAs have been performed on a specific metal like silver or gold, focusing on the visible or near-infrared (IR) spectral regions, as the ultraviolet (UV) region with such metals is limited by interband transitions. The UV region is especially interesting as it covers the absorption region of many chiral biomolecules [36].

In this work, we investigate intrinsically chiral optical effects – specifically absorption CD at normal incidence – in ENHAs with square lattice realized in thin films of silver, gold, and aluminum on glass. Our purpose is twofold: first, we aim at clarifying the origin of CD and its relation to SPP properties upon symmetry reduction in the plasmonic metasurface. Second, we optimize the parameters for CD enhancement, with specific attention on aluminum in the visible-near UV spectral range. The choice of the square lattice (as compared to our previous study on ENHA in Au with a triangular lattice [31]) yields a more complete picture of chiral properties in ENHAs, and it allows comparing the results of two different simulation methods under ideal conditions, as discussed below. The results shed light on the subtle interplay between two concurring mechanisms of symmetry reduction, namely elliptical nanohole shape and tilting of nanohole axis with respect to the symmetry axes of the array. Moreover, they give guidelines for optimizing the CD from the near-IR (using Au or Ag) to the UV spectral region (using Al metal). Thus, the present work sets the bases for applications of the ENHA to chiroptical spectroscopies, notably in the near-UV region which is especially interesting for various kinds of biomolecules.

2. Structure and method

In the sketches of Fig. 1(a,b), we show the metasurface with the array of elliptic nanoholes used in our study. A metal layer of thickness t is embedded between SiO_2 and air. A square lattice of period a, consisting of elliptical holes, is etched in the metal layer. The short and long diameters of each hole are denoted by D_1 and D_2, respectively. We define the angle ϕ between the y-axis and the longer nanoellipse axis. The nanostructure is excited from the top (air side) with a plane wave under normal incidence.

When the elliptical holes are aligned along a symmetry axis of the square lattice (i.e., for $\phi = 0, 45°, 90°, \ldots$), the ENHA has vertical mirror symmetries and is non chiral. However, when the elliptical holes are tilted with respect to the symmetry axes (see the 2D view in Fig. 1(b)), the metasurface cannot be superposed onto its mirror image by any symmetry plane. Indeed, while each elliptical hole alone is obviously achiral, the lattice arrangement with tilted holes breaks mirror symmetries with respect to the minor and major axes, so that the single unit cell

Optics EXPRESS

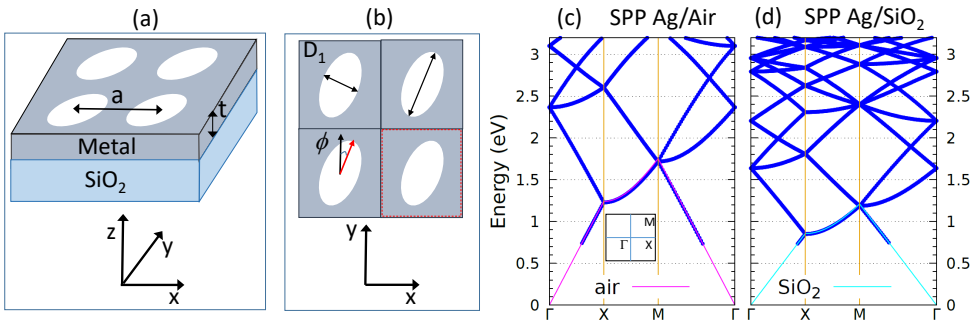

Fig. 1. (a,b) Sketch of the metasurface studied in this work with 3D view (a) and 2D view (b), with the 2D unit cell shown by red lines. (c,d) Dispersion of the surface plasmon polaritons at the Ag/air (c) and Ag/glass (d) interface, folded in the first Brillouin zone of the square lattice (see inset in (c)), for a lattice constant $a = 500$ nm.

of the square lattice (indicated by red lines in Fig. 1(b)) and the full ENHA have no vertical mirror symmetries. Furthermore, the presence of the glass substrate breaks mirror symmetry with respect to the horizontal (xy) plane, so that the structure is indeed 3D chiral according to the general definition [8,10,15,19]. Thus, our metasurface structure interacts in a different way with right- and left- circularly polarized light, giving rise to intrinsic chiral effects like optical activity and circular dichroism even at normal incidence. Since the chirality of the structure follows from the interplay between each elliptical nanohole and the lattice arrangement, we expect strong lattice effects in the chiroptical properties. Subtle phenomena like the difference between 2D and 3D chirality, nonreciprocal transmission of circularly polarized light, and similar, have been discussed in the literature [37,38] and are outside the scope of the present work.

The optical properties of elliptic nanoholes are numerically investigated by using two approaches. We employ the 3D Finite Difference Time Domain (FDTD) method using Lumerical-Ansys commercial simulator by setting perfectly matched layers in the z-direction and periodic boundary conditions in x and y directions. Meanwhile, we apply Bloch-mode scattering matrix method in the open-source software known as EMUstack, where a finite element approach is used to calculate the Bloch-modes in each 2D layer of the proposed structure and the electromagnetic field is propagated using a scattering matrix [39,40]. Both mentioned methods allow calculating transmittance (T), reflectance (R), absorbance (A), and field profiles. We focus on the CD in absorption, which is defined as usual by

$$\mathrm{CD}_A = \frac{A_{lcp} - A_{rcp}}{A_{lcp} + A_{rcp}}. \tag{1}$$

Moreover, in both techniques, a square unit cell is used to implement the square lattice. We consider elliptical nanoholes etched in three different metals Ag (dielectric function measured in [30]) and Au, Al (dielectric function in Lumerical database, taken from Ref. [41]. The optical functions of the three metals are shown in the Appendix. Glass is assumed to be lossless with a refractive index of 1.45.

Before presenting the numerical results for the optical properties, in Fig. 1 we show the dispersion of SPPs at a planar Ag/air interface (Fig. 1(c)) and Ag/glass interface (Fig. 1(d)). These results are obtained from the usual SPP dispersion relation [4]

$$ck = \omega\sqrt{\frac{\varepsilon_1\varepsilon_2}{\varepsilon_1 + \varepsilon_2}}, \tag{2}$$

where $\varepsilon_1, \varepsilon_2$ are the dielectric functions (relative permittivities) of the two media, by folding the calculated SPP dispersion in the first Brillouin zone of the square lattice with period $a = 500$

Optics EXPRESS

nm. The lowest SPP states at the Γ point lie around $E = 2.366$ eV ($\lambda \simeq 524$ nm) at the Ag/air interface, and around $E = 1.638$ eV ($\lambda \simeq 757$ nm) as well $E \simeq 2.2$ eV ($\lambda \simeq 564$ nm) at the Ag/glass interface. Such states couple to electromagnetic radiation at normal incidence and give rise to resonances in absorption, as we will show in the following.

3. Physical origin of absorption resonances and circular dichroism

In this section, we wish to unravel the physical origin of circular dichroism in the ENHA. For this purpose, we focus on Ag metasurface and we fix the metal thickness and lattice constant to $t = 100$ nm and $a = 500$ nm, respectively.

We first calculate the transmission and absorption spectra starting from circular holes and introducing a hole ellipticity E defined as

$$E = \frac{D_2 - D_1}{D_1}. \tag{3}$$

In Fig. 2 we show the spectra for fixed $D_1 + D_2 = 600$ nm as a function of the ellipticity, for untilted holes ($\phi = 0$), using linear polarization along the short and long axis of the holes. For the case $E = 0$, the holes are circular with $D_1 = D_2 = 300$ nm, and transmission spectra display a broad EOT peak, which is interrupted by two lattice-related minima at $\lambda = 515$ nm and $\lambda = 740$ nm. These two minima originate from excitation of the SPPs related to the Ag/air and Ag/SiO_2 interfaces [1,2]: indeed, the two wavelengths are very close to the lowest resonances appearing at the Γ point in Fig. 1(c) and (d), respectively. The small discrepancy can be attributed to numerical accuracy of the FDTD simulation and to the approximation of calculating the SPP for the planar interface. Two absorption peaks are also observed at wavelengths $\lambda = 545$ and 800 nm, slightly higher than those of transmission minima but still related to the SPP at the two interfaces. Moving from circular to elliptical holes, the EOT peaks for the two orthogonal polarizations are split, with a distinct dependence on ellipticity. We can observe that transmission peaks for polarization along the short axis of the holes are red-shifted compared to polarization along the long axis. On the other hand, the transmission peaks for polarization along the long axis are slightly blue-shifted and become considerably narrower. Similar observations of anisotropic behavior for nanoholes with elliptical [42,43] or rectangular shape [44,45] were made previously. We attribute this phenomenon to a retardation effect: the oscillating SPP for polarization along the short axis is subject to a stronger retardation, and it acquires a red-shift, as it radiates mainly along the perpendicular (long axis) direction. On the other hand, the SPP for polarization along the long axis is subject to a weaker retardation when increasing the ellipticity, leading to a peak narrowing and a blue-shift. The absorption peaks are also split when moving from circular to elliptical holes, and the splitting grows with the ellipticity (i.e., with the anisotropy) of the holes. The splitting of both EOT and absorption peaks are maximum when $E = 1$, which corresponds to diameters $D_1 = 200$ nm, $D_2 = 400$ nm.

In Fig. 3 we consider the case of elliptical holes ($D_1 = 200$ nm, $D_2 = 400$ nm) that are either untilted ($\phi = 0$) or tilted along a non-symmetry direction ($\phi = 22.5°$) with respect to the square axes. Linearly polarized absorption and transmission spectra for the untilted holes (Fig. 3(a,d)) are identical to those of Fig. 2 for the corresponding values of the diameters, i.e., when the ellipticity $E = 1$. Circularly polarized spectra for the untilted holes (Fig. 3(b,e)) are the same for RCP and LCP (no circular dichroism, see Fig. 3(c)), and they comprise the features of linearly polarized spectra with polarizations along the short and long axes. When the holes are tilted, instead, circularly polarized spectra become different for RCP and LCP. This gives rise to a circular dichroism in absorption (Fig. 3(c)), whose maximum absolute value is almost 30% in the considered spectral range. This is a proof of intrinsic chiral behavior of the ENHA due to symmetry breaking. Moreover, the chirality is peaked in the spectral ranges around the

Optics EXPRESS

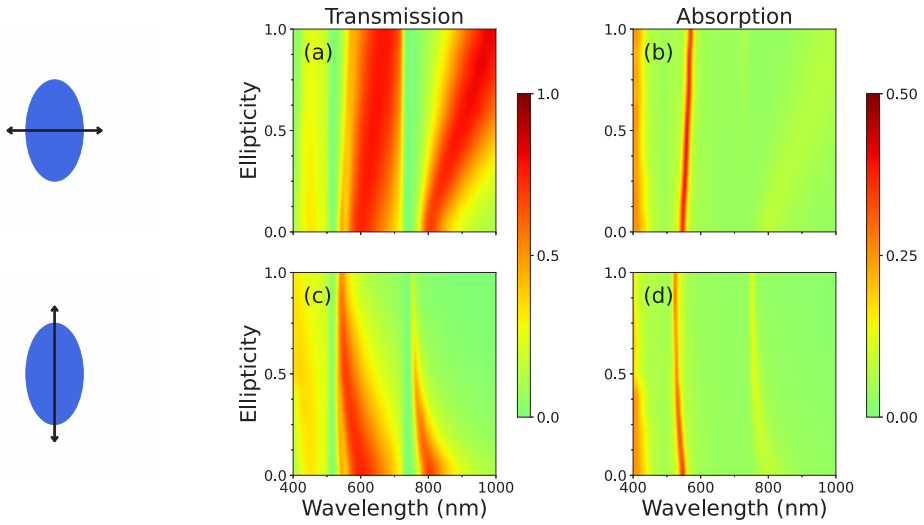

Fig. 2. Transmission and absorption spectra for untilted holes, for an Ag film with thickness $t = 100$ nm, lattice constant $a = 500$ nm, for fixed $D_1 + D_2 = 600$ nm, as a function of the ellipticity E (see text; for $E = 0$, the holes are circular with $D_1 = D_2 = 300$ nm, while for $E = 1$ the holes have diameters $D_1 = 200$ nm, $D_2 = 400$ nm). Upper panels: (a) transmission and (b) absorption for polarization along the short axis. Lower panels: (c) transmission and (d) absorption for polarization along the long axis.

SPP excitations, which means that CD in absorption is related to the corresponding resonant absorption behavior.

To analyze the effect of chiral symmetry breaking, we further report on the dependence of CD on the tilting angle. As we can see from Fig. 3(f), on increasing ϕ from 0°, the CD increases and it reaches a maximum of $\sim 45\%$ at ϕ close to 22.5°, then it vanishes at $\phi = 45°$. For larger tilting angles the CD inverts sign: CD$(90 - \phi)$=−CD(ϕ). Therefore, the same structure, when properly oriented, can give CD of opposite behavior. Metasurfaces with this feature can be regarded as plasmonic enantiomers. In the following, we denote the first CD peak at shorter wavelengths ($\lambda \simeq 520 - 580$ nm) as Peak 1, and the second peak at longer wavelengths ($\lambda \simeq 720 - 760$ nm) as Peak 2. Notice that in Fig. 3(f) peak 1 is always stronger than peak 2: this is not a general feature, as the relative strengths of the two peaks can be reversed by proper optimization, as we show later.

To further investigate the relation between absorption and SPPs, as well as the origin of CD, in Fig. 4 we show the xz and yz cross-sections of the intensity enhancement of the electric field at $\phi = 0$ for the cases in Fig. 3(a,d), for the wavelengths of maximum absorption (arrows in Fig. 3(a)) and of minimum transmission (arrows in Fig. 3(d)). At the wavelengths of maximum absorption, the electric field is strongly confined and enhanced at one or both interfaces. On the other hand, no or little enhancement occurs at the wavelength of minimum transmission. Looking at Fig. 4 in more detail, for polarization along the long axis of the nanoholes, the field at the wavelength of maximum absorption is strongly enhanced (1) at the top interface for peak 1, and (2) at the bottom interface for peak 2. This agrees with the folded SPP dispersions shown in Fig. 1 (b,c), which indicate that the SPP at the metal/air (metal/glass) interface is responsible for enhanced absorption in the case of peak 1 (peak 2). The case of polarization along the short axis is more complex, especially for peak 1 at $\lambda = 571$ nm, which displays field enhancement at the top and bottom interfaces. We attribute this to the fact that this wavelength is close to the second resonance at the Γ point for the SPP at the metal/glass interface in Fig. 1(d), which has an energy $E \simeq 2.2$ eV. Thus, SPPs at both interfaces are involved, which explains a field enhancement at top

Optics EXPRESS

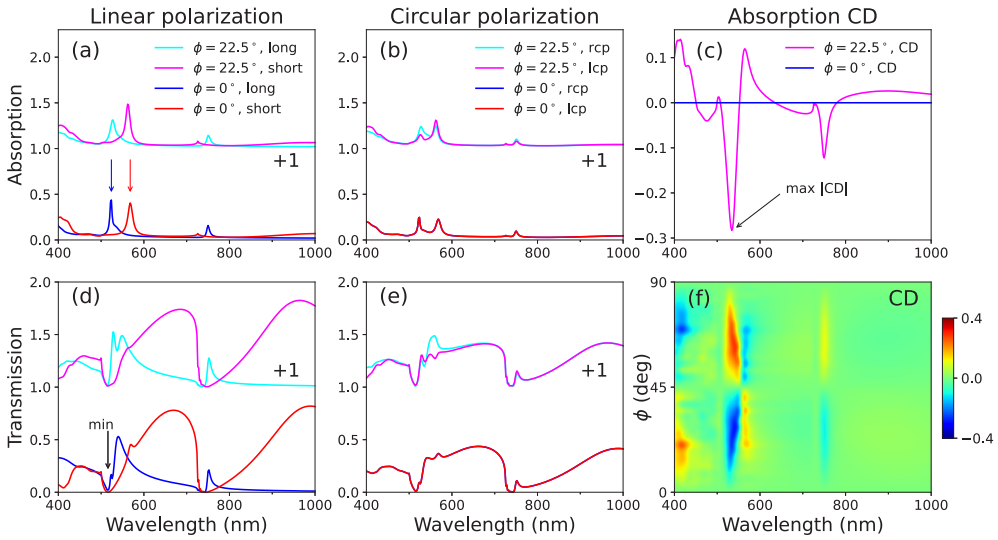

Fig. 3. Panels (a), (b): absorption spectra for tilting angle $\phi = 0$ (unshifted) and for $\phi = 22.5°$ (shifted), for linear polarizations along the short and long axes of the holes (a) and for right- or left circular polarizations (b). Panel (c): absorption CD for $\phi = 0$ and $\phi = 22.5°$. Panels (d), (e): transmission spectra for tilting angle $\phi = 0$ (unshifted) and for $\phi = 22.5°$ (shifted), for linear polarizations along the short and long axes of the holes (d) and for right- or left circular polarizations (e). Panel (f): map of the absorption CD for tilting angle ϕ increasing from 0 to 90°. Parameters: Ag film with thickness $t = 100$ nm, lattice constant $a = 500$ nm, diameters $D_1 = 200$ nm, $D_2 = 400$ nm.

and bottom surfaces. This interpretation is in line with the model of [5], which shows that EOT occurs via coupling to the localized SPP of the nanoholes.

On the whole, the results of Fig. 4 confirm that strong SPP resonances are excited at the wavelength of maximum absorption. More details are given in the Appendix, where we discuss the local absorption density inside the metal. Also, we prepared videos that allow visualizing the 3D profile of $|E|^2$ at all wavelengths. Parameters for the Ag ENHA are the same as for Fig. 4 with excitation polarized along the short (Visualization 1) and long (Visualization 2) axis of the ellipse, respectively. The videos show clearly the resonance effects on the electric field when the wavelength is scanned across the absorption/transmission resonances.

When the nanoholes are tilted, such resonances acquire a chiral character and give rise to the strong CD enhancement shown in Fig. 3. We explore the origin of this phenomenon in Fig. 5, where we show a dynamic analysis of the electric field component at $\phi = 22.5°$, for linear polarization along long or short axis when the structure is excited at 541 nm (the wavelength of maximum |CD| as indicated in Fig. 3(c) by an arrow). The physical mechanism of CD is apparent when visualizing the color frames, that correspond to the two linear polarizations that are dephased by ±90°. Then, the fields corresponding to linear polarizations along long and short axes sum up with a phase delay of −90° (LCP) or +90° (RCP). In the case of tilted holes, there is a symmetry breaking that introduces a difference between the sums for LCP and RCP, respectively. Thus, the physical mechanism of CD is traced back to a subtle unbalance in the interference of the field amplitudes for light polarized along the long and short axes of the tilted nanoholes. It is interesting to notice that such symmetry breaking can give rise to large |CD| values by proper optimization, as we discuss in the next section.

It is worth investigating to which extent the CD peaks depend on the geometrical parameters of the elliptical holes. We have already seen in Fig. 3(f) that the peak wavelength does not depend

Optics EXPRESS

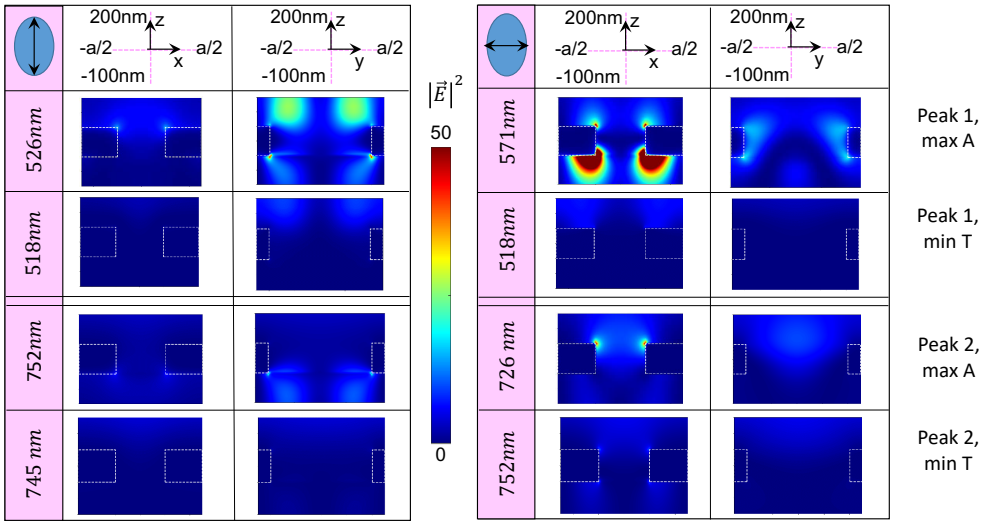

Fig. 4. Electric field intensity monitored in xz ($y = 0$), and yz ($x = 0$) planes, for polarizations along long and short axis of the nanohole ellipse.We display its confinement at different wavelengths, which are of interest for maximum absorption or minimum transmission, as shown in Fig. 3. Units: $|E|^2$ in V^2/m^2, for an incident field $E = 1$ V/m. The hole profiles are indicated by thin white lines. The Ag-ENHA parameters are: thickness $t = 100$ nm, lattice constant $a = 500$ nm, diameters $D_1 = 200$ nm, $D_2 = 400$ nm, untilted holes ($\phi = 0$).

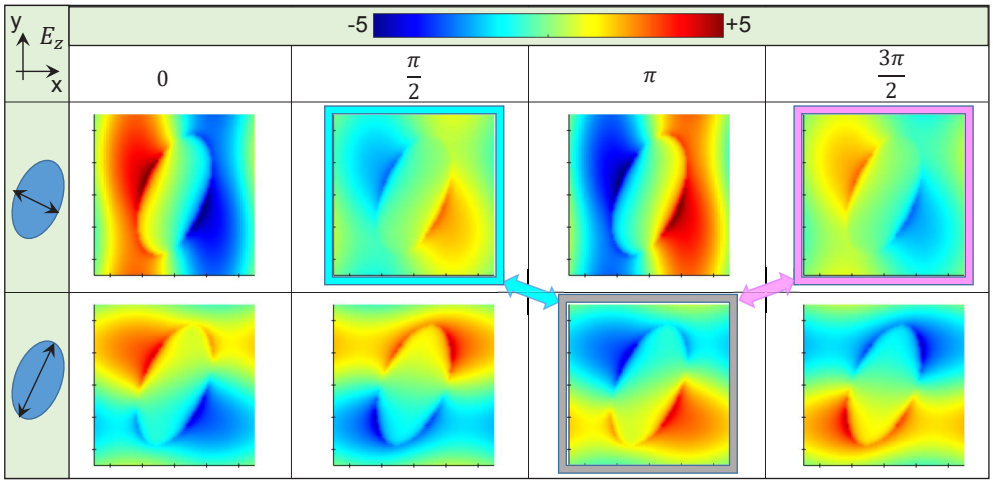

Fig. 5. Dynamic field investigations for tilted holes ($\phi = 22.5°$) revealing physical mechanism of CD; we monitor the behavior of E_z component over one period of time, when the Ag-ENHA is excited at 541 nm (the wavelength of maximum |CD| as indicated in Fig. 3 (c)), by linear polarization along short (top panels) and long (low panels) ellipse axis. The colored frames correspond to the phase offset of $-90°$ (cyan) and $+90°$ (magenta) between the two linear polarizations, which in the interference gives RCP and LCP, respectively. Units: E_z in V/m, for an incident field $E = 1$ V/m. Fields are monitored at 10nm above Ag-ENHA with Ag thickness $t = 100$ nm, lattice constant $a = 500$ nm, diameters $D_1 = 200$ nm, $D_2 = 400$ nm.

Optics EXPRESS

on the tilting angle. In Fig. 6 we show CD maps for tilting angle $\phi = 22.5°$ in two cases: (a) for fixed $D_1 + D_2 = 600$ nm as a function of ellipticity E, and (b) for fixed $D_2 = 500$ nm as a function of small hole diameter D_1. In both cases we see that the CD peak wavelength is nearly independent of the ellipse parameters. Indeed, the chiral response of the present metasurface based on ENHA array results from a lattice effect that breaks mirror symmetries of the isolated nanoholes (see discussion in Sec. 2). We will show in the next Section that the wavelength of CD peaks can be effectively tuned by varying the lattice constant of the array, which determines the resonance energies of folded SPP modes in Fig. 1(c,d).

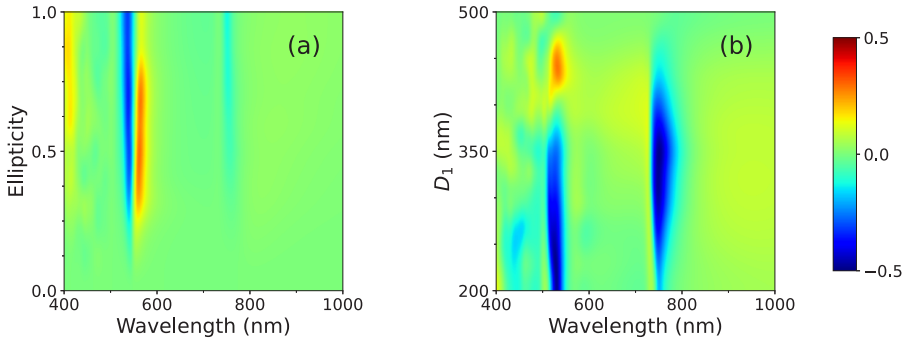

Fig. 6. Map of the absorption CD for a Ag film with thickness $t = 100$ nm, lattice constant $a = 500$ nm, tilting angle $\phi = 22.5°$. Panel (a): fixed $D_1 + D_2 = 600$ nm, as a function of the ellipticity E. Panel (b): fixed $D_2 = 500$ nm, as a function of D_1.

Summarizing, the physical origin of CD in the ENHA can be described as follows. The anisotropy of the elliptical holes splits the EOT and the absorption resonances into distinct peaks, which correspond to linear polarizations of the incident field along the short and long axes of the ellipse. The absorption peaks are associated with excitation of SPPs at the metal/air or at the metal/glass interfaces. When the elliptical nanoholes are rotated with respect to the symmetry axes of the square lattice, the contributions to absorption arising from the two linear polarizations add up with a phase delay, with an unbalance between left- and right circular polarizations, giving rise to chiral behavior with CD resonances in correspondence with the absorption peaks.

4. Optimization of circular dichroism from the near-IR to the UV

The goal of this Section is to optimize the CD in absorption with respect to geometrical parameters of the nanoholes, and to explore the dependence on film thickness and on the lattice constant, in order to achieve robust CD resonances from the near-IR to the UV spectral range. In addition to the noble metals Ag and Au, we consider also the case of Al, which is an interesting candidate for use in the UV range due to the absence of interband transitions in the near UV.

To this purpose, in Fig. 7 we present the results of a full CD optimization done in EMUstack based on a differential evolution algorithm with 3 parameters: hole diameters D_1 and D_2, hole tilting angle ϕ for the three metals Ag, Au, and Al. For each metal layer, we optimize the CD for the peak at shorter wavelength (peak 1, related to the SPPs at both interfaces) and the one at longer wavelength (peak 2, mostly related to the SPP at the metal/SiO_2 interface). The final parameters are shown in Table 1. In order to compare different computational methods, in Fig. 7 we show CD spectra calculated with both EMUstack and FDTD using the optimized parameters. The results show generally very good agreement. Small discrepancies especially for peak 1 in gold are attributed to a large and rapidly varying imaginary part of the dielectric function in the spectral region of interband transitions, which makes both methods very sensitive to the precise computational parameters like mesh size, perfectly matched layers, etc.

Optics EXPRESS

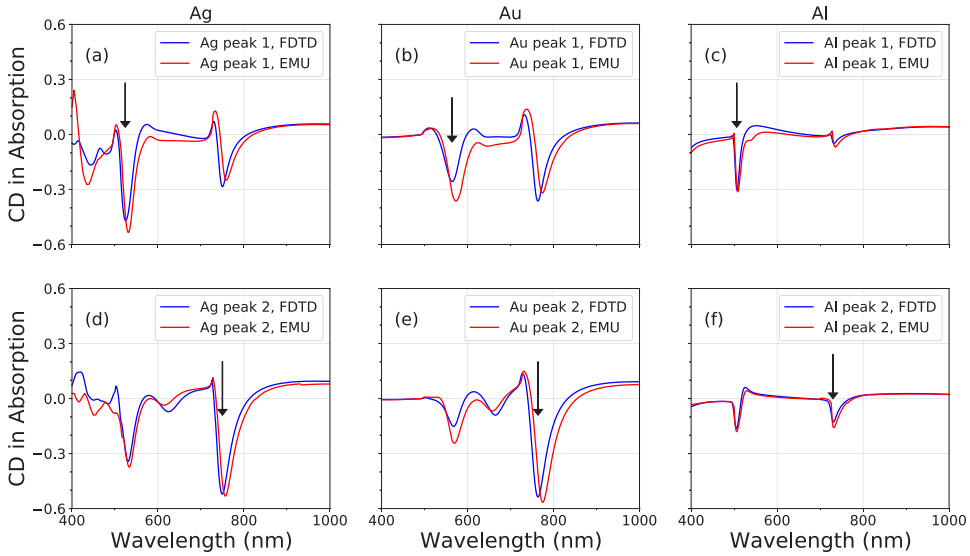

Fig. 7. Absorption CD spectra for different metals (Ag, Au, Al), with optimized parameters for the first peak at shorter wavelengths (upper panels, see arrows) or for the second peak at longer wavelengths (lower panels, see arrows). Comparison between EMUstack results (red lines) and FDTD (blue lines). Parameters: t = 100 nm, a = 500 nm, hole diameters and tilting angles are given in Table 1 of the text.

Table 1. Optimized parameters for the spectra shown in Fig. 7.

Material and peak	Ag	Au	Al	Ag	Au	Al
	Peak 1	Peak 1	Peak 1	Peak 2	Peak 2	Peak 2
D_1 (nm)	228.94	229.36	234.71	320.2	304.44	323.42
D_2 (nm)	499.94	499.78	498.08	499.88	496.02	451.22
ϕ (deg)	26.10	25.77	21.19	15.27	15.97	22.44

As shown in Fig. 7, the optimization leads to substantial CD values ($|\mathrm{CD}|_{\max}$ >50%) for silver and gold, with peak 2 being generally stronger than peak 1, making both metals suited for operation in the visible (λ>500 nm for Ag, λ>600 nm for Au) or in the near-IR. For the Al metal instead, peak 1 is stronger than peak 2, mainly because of the interband transition of Al that takes place around λ = 800 nm. This makes Al more suitable in the visible-UV (working at sufficiently short wavelengths to be far from the interband transition).

The electromagnetic field behavior can be visualized as a 3D absorption density ρ_{abs} in the unit cell. Considering the case of Ag, in Fig. 8(a) we show the absorption density for LCP and RCP excitation at the wavelength 532 nm of peak 1 for the optimized parameters in Fig. 7(a). The RCP excitation gets more absorbed, as it is evident from the edges of the nanoholes in the bottom right corner of Fig. 8(a). This results in a negative CD (as seen in Fig. 7), which again follows from SPP enhancement at the metal/air interface. In Fig. 8(b) instead, we perform a sweeping analysis over Ag film thickness keeping the same optimized D_1, D_2, and ϕ as in Fig. 7(a). The resonance wavelengths of CD peaks are almost unchanged, as they follow from a lattice effect. The CD of peak 1, which is associated with the metal/air interface, has a weak dependence on film thickness with a maximum remaining close to 55%. The CD of peak 2 instead decreases with increasing film thickness, as the resonance effect on the metal/SiO_2 interface becomes less pronounced.

Optics EXPRESS

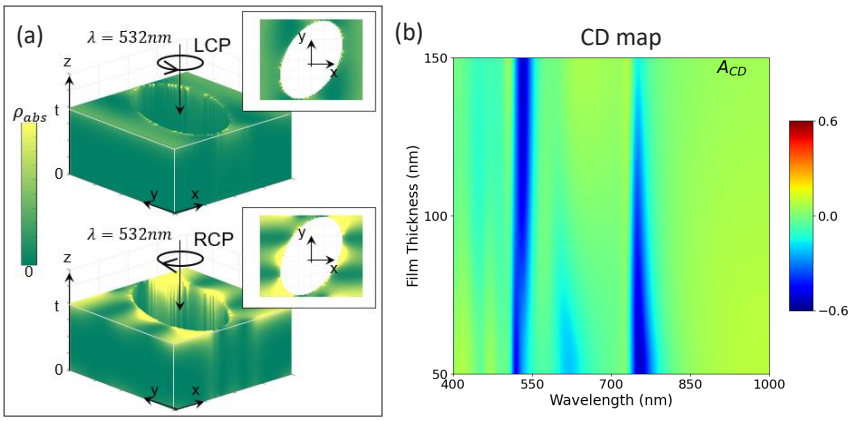

Fig. 8. Results for Ag: (a) 3D absorption density ρ_{abs} confinement in a unit cell, for LCP and RCP excitation at the wavelength of peak 1 for the optimized parameters in Fig. 7(a); 2D inset panels show the top surface view. (b) Absorption CD map as a function of Ag film thickness, keeping the same D_1, D_2, ϕ as in Fig. 7(a).

Finally, we wish to investigate the dependence of CD on the lattice constant, especially in order to explore the near-UV spectral region that is highly relevant for chiral sensing of various species of biomolecules. To this goal, in Fig. 9 we consider an Al film of fixed thickness 100 nm and we perform a sweep over the lattice constant by keeping constant ratios $D_1/a, D_2/a$ and hole tilting angle (the values as indicated in the caption follow from an optimization at lattice constant a = 350 nm). As expected, decreasing the lattice constant leads to a shift in absorption and CD peaks towards the ultraviolet range. In Fig. 9(a,b) the interband transition of Al around $\lambda \sim 800$ nm is clearly apparent, together with the absorption peaks that give rise to the CD peaks in Fig. 9(c). Notably, the peak value of |CD| is strongly increased when reducing the lattice constant and shifting the peak to the UV, resulting in a maximum value $|\text{CD}|_{\text{max}} \simeq 40\%$.

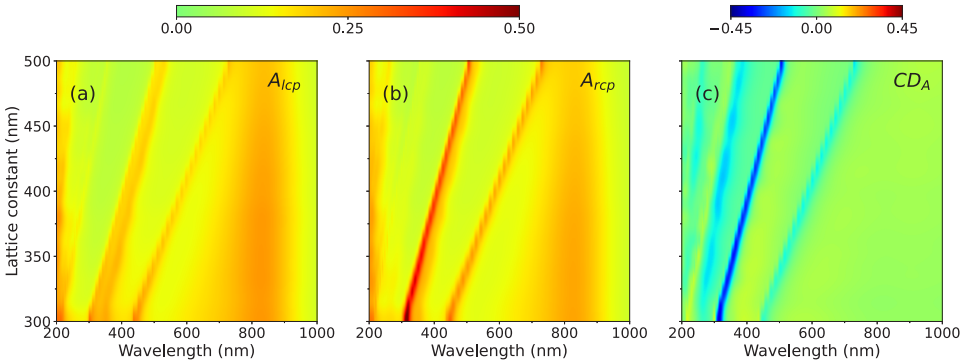

Fig. 9. (a) Absorption spectra for LCP, (b) absorption spectra for RCP, (c) CD in absorption for an Al film of thickness t = 100 nm as a function of lattice constant a, keeping constant values $D_1/a = 0.5565$, $D_2/a = 1$, $\phi = 20.95°$.

It is interesting to notice that besides the two SPP peaks that we dealt with up to now, additional SPP peaks show up on the short-wavelength side in Fig. 9(c). Such peaks are associated with higher-order SPP modes folded at the Γ point (like for the case of Ag in Fig. 1(b,c)). These results confirm the interest of using Al metal in the near-UV spectral region and will be the basis for future work towards exploring absorption CD for chiral sensing in the ultraviolet range.

Optics EXPRESS

5. Conclusions

In conclusion, we investigated chiral properties of square 2D elliptic nanohole arrays in three different metallic metasurfaces made of Ag, Au, and Al, from the near-infrared to the ultraviolet spectral range. The elliptical nanohole array with tilted holes on a glass substrate is an intrinsically chiral lattice, giving rise to circular dichroism which is closely related to extraordinary optical transmission through the nanoholes, and it is resonantly enhanced at absorption peaks due to surface plasmon polariton (SPP) resonances at the metal/glass and metal/air interfaces. The elliptical shape of the nanoholes splits the absorption peaks at each SPP resonance, while tilting of the nanohole axis produces an unbalance between the fields originating from linear polarizations along the long and short axes: they sum up with a phase delay of -90° (LCP) or +90° (RCP), ending up in a CD for tilted holes and explaining the strongly dispersive features of CD spectra. We then performed a full optimization on the geometry parameters, leading to substantial CD values ($|CD|_{max} > 50\%$) for silver and gold leading to suitable use in visible or near-IR, and ($|CD|_{max} > 40\%$) for aluminum leading to suitable use in the visible and ultraviolet. The CD resonance wavelengths have a minor dependence on the ellipse parameters, as they follow from a lattice effect, and can be effectively tuned via the lattice constant. The benchmark of the two computational electromagnetic tools EMUstack and FDTD leads to a good agreement of the spectra and supports the reliability of the results. Plasmonic metasurfaces made of an Al film stands up as a promising candidate to achieve large |CD| in the near-UV region, possibly with the addition of a thin oxide layer to prevent oxidation of the top surface. Absorption and CD spectra of Al films at wavelengths below the interband transition display a number of features that arise from folded SPP modes.

These findings can be further pursued for deeper investigations of plasmonic light-matter coupling, as well as for applications to chiral sensing of biomolecules with resonances in the visible or near-UV spectral range. On the fundamental side, a deeper study of folded SPP resonances at normal and oblique incidence is interesting and would best be performed on Al films in the UV region. Another possible extension is to add a mirror at the bottom of the structure: this could boost the chiral CD response [46] and/or facilitate the observation of chiral effects in diffraction [47,48]. Finally, it is known that chiral sensing is best performed in a configuration in which the local chiral response is enhanced, while the global response is achiral [15,49–51]: this allows to enhance the interaction between chiral molecules and the medium, while avoiding to mask the small chiroptical response of the analyte by a large background signal. A simple way to achieve this in our ENHA metasurface is to introduce a supercell with several unit cells, in which the elliptical nanoholes are tilted by complementary angles yielding zero net CD but still a locally chiral response. Combining such an extended structure with calculations of the local chirality enhancement is a promising approach towards applications of the ENHA to actual chiral sensing applications.

6. Appendix

6.1 Dielectric functions of the metals

In Fig. 10 we show the dielectric functions used in calculating the optical properties of the three metals. These are further interpolated in the software we use for the numerical calculations.

For the noble metals, the onset of interband transitions at short wavelengths is clearly apparent. The optical spectrum of Ag is free of interband transitions in the whole visible region, while the spectrum of Au is free of interband transitions for wavelengths larger than ~ 600 nm. The optical spectrum of Al is characterized by an interband transition around 800 nm, while for shorter wavelengths the dielectric function is smooth with a decreasing imaginary part, making it a suitable candidate for applications in the UV region.

Optics EXPRESS

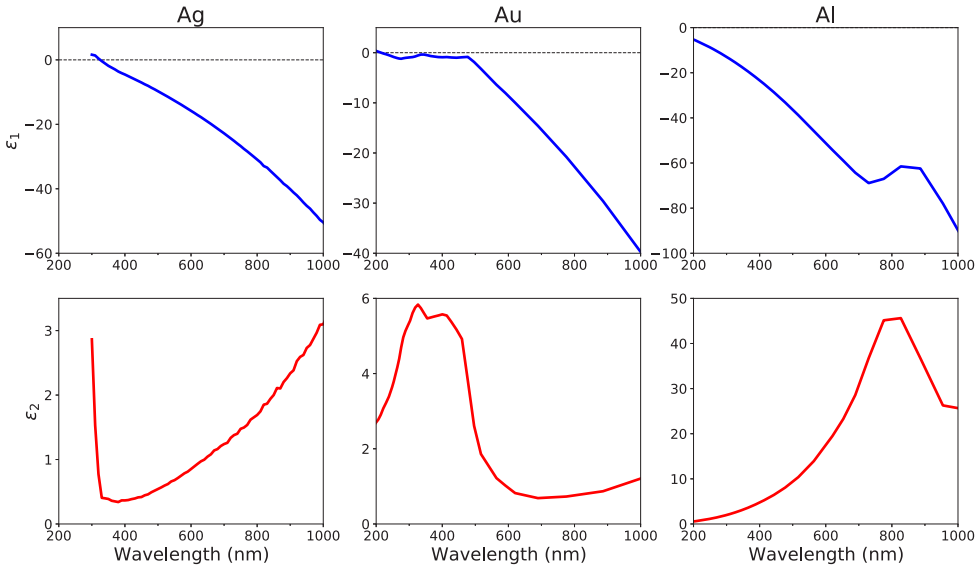

Fig. 10. Real and imaginary parts of the dielectric function for the three metals considered in this work. Data for Ag are taken from Ref. [30], while data for Au and Al are in the Lumerical database and are taken from Ref. [41].

6.2 Electric field enhancement and absorption density

In Sec. 3 we discussed the physical origin of CD in the investigated metasurfaces. Here we present further results to illustrate the relation between SPP resonances and absorption enhancement. We adopt the same parameters as in Fig. 4, namely, we consider Ag film of thickness $t = 100$ nm and a nanohole array with lattice constant $a = 500$ nm and untilted holes ($\phi = 0$) with diameters $D_1 = 200$ nm, $D_2 = 400$ nm.

In Fig. 11 we show the local absorption density inside the metal, which is given by $P_{\text{abs}} = 0.5\omega\varepsilon_2(\omega)|E|^2$. We plot P_{abs} for polarizations along the long and short axes of the nanoholes, taking the wavelengths of maximum absorption in Fig. 3(a). We can notice the presence of resonances at the hole sidewalls and, generally, at the top and bottom interfaces.

However, such plots give only a partial view of the spatial regions where absorption is actually occurring. To clarify this point, in Fig. 12 we show absorption spectra obtained by integrating the absorption density in the upper and lower halves of the metal layer, respectively. It can be seen from Fig. 12(a) that in the case of peak 1, absorption is dominated by the upper part of the metal: this agrees with the fact that such absorption peak originates mostly from the SPP at the metal/air interface (e.g., the resonance at 2.366 eV in Fig. 1(c)). On the other hand, in the case of peak 2, absorption is dominated by the lower part of the metal and can be attributed to a resonance with the SPP at the metal/glass interface (the resonance at 1.638 eV in Fig. 1(d)).

The case of polarization along the short axis is more complex, as peak 1 is clearly dominated by the bottom half of the metal. This can be explained by two reasons: (i) looking at the spectra in Fig. 3, the maximum absorption of peak 1 occurs at a wavelength of high transmission for such a thin metal film (unlike for polarization along the long axis, where the absorption maximum coincides with a minimum of transmission); (ii) the absorption maximum occurs at a wavelength $\lambda = 571$ nm, which is close to the second SPP resonance at the metal/glass interface (the resonance around 2.2 eV in Fig. (1d)). Thus, the electromagnetic wave incident on the metal interacts preferentially with the SPPs at the metal/glass interface.

Optics EXPRESS

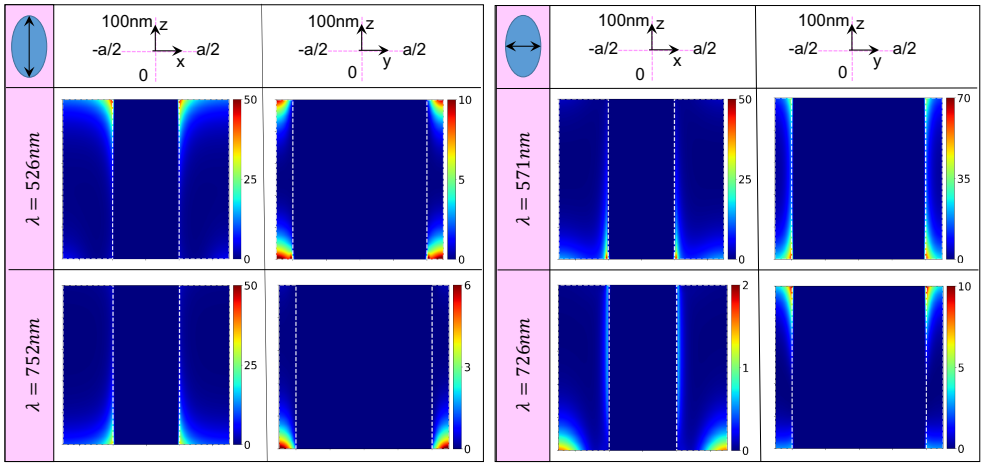

Fig. 11. Power absorption density (normalized to the source power, in units of 10^{19}) in the Ag film, monitored in xz ($y = 0$), and yz ($x = 0$) planes, for polarizations along long and short axis of the nanohole ellipse. The hole profiles are indicated by thin white lines. The Ag-ENHA parameters are the same as in Fig. 4, and the chosen wavelengths are those of maximum absorption.

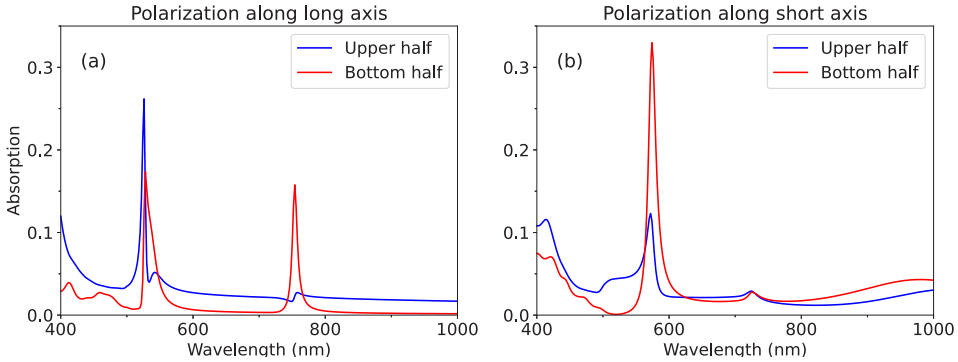

Fig. 12. Absorption spectra in the Ag metasurface, calculated in the upper half (50 nm < z <100 nm) and in the lower half (0<z<50 nm) of the metallic film, for (a) polarization along the long axis, and (b) polarization along the short axis of the nanoellipse. The Ag-ENHA parameters are the same as in Fig. 4.

6.3 Local electric and magnetic field profiles

While the results of Fig. 5 demonstrate that the CD is intimately related to phase effects in dynamic field evolution, it is also useful to analyze the chiral response from the point of view of local profiles of electric and magnetic fields. In Fig. 13 we show the real parts of field components E_z, H_z in a xy plane just above the top Ag surface, for both circular polarizations of incident light, in the cases of untilted holes (non-chiral lattice) and tilted holes (chiral lattice). While in the case of untilted holes RCP and LCP polarizations have corresponding field profiles, when the holes are tilted we can see the emergence of a clear asymmetry between the fields for RCP and LCP excitation. Thus, the chiral nature of the metasurface structure is related to a dissymmetry in the local fields that are produced by excitation with circularly polarized light.

Optics EXPRESS

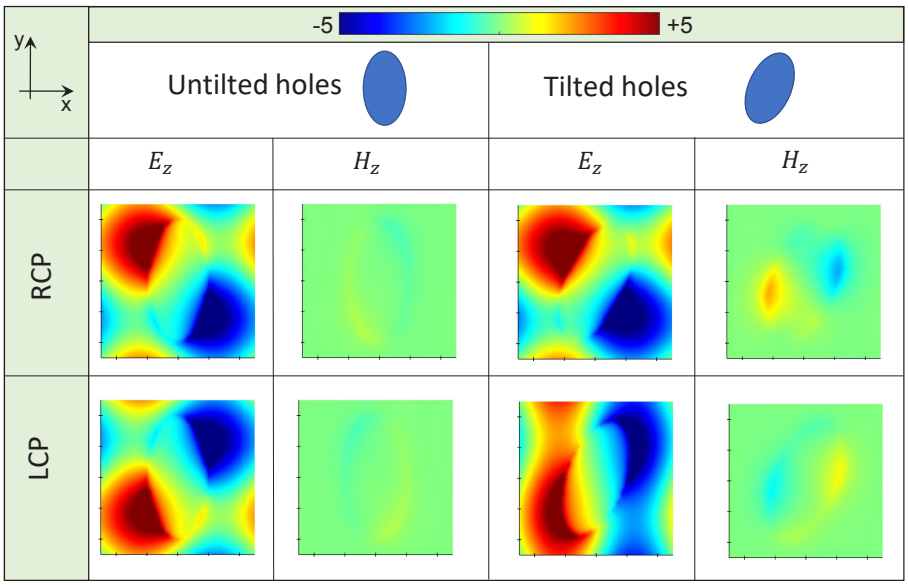

Fig. 13. Electric and magnetic fields E_z, H_z (real parts), monitored in xy plane 10 nm above the top surface of the Ag film, for right- and left-circular polarization of the incident beam, in case of untilted ($\phi = 0$) and tilted $\phi = 22.5°$ elliptical holes. The wavelength is $\lambda = 541$ nm, which corresponds to the maximum CD in Fig. 3(c) and to Fig. 5, and the other Ag-ENHA parameters are also the same as in Fig. 5.

Funding. Ministero dell'Istruzione, dell'Università e della Ricerca (2017 PRIN project 2017MP7F8F-004 "NOMEN").

Disclosures. The authors declare no conflicts of interest.

Data availability. Data obtained in this work are not publicly available at this time but may be obtained from the authors upon reasonable request.

References

1. T. Ebbesen, H. Lezec, H. Ghaemi, T. Thio, and P. Wolff, "Extraordinary optical transmission through sub-wavelength hole arrays," Nature **391**(6668), 667–669 (1998).
2. F. García de Abajo, "Colloquium: light scattering by particle and hole arrays," Rev. Mod. Phys. **79**(4), 1267–1290 (2007).
3. W. Barnes, A. Dereux, and T. Ebbesen, "Surface plasmon subwavelength optics," Nature **424**(6950), 824–830 (2003).
4. S. A. Maier, *Plasmonics: Fundamentals and Applications* (Springer, 2007).
5. H. Liu and P. Lalanne, "Comprehensive microscopic model of the extraordinary optical transmission," Nature **452**(7188), 728–731 (2008).
6. N. Meinzer, W. Barnes, and I. Hooper, "Plasmonic meta-atoms and metasurfaces," Nat. Photonics **8**(12), 889–898 (2014).
7. Z. Wang, J. Chen, S. Khan, F. Li, J. Shen, Q. Duan, X. Liu, and J. Zhu, "Plasmonic metasurfaces for medical diagnosis applications: A review," Sensors **22**(1), 133 (2021).
8. L. Kelvin, *The Molecular Tactics of a Crystal* (Clarendon, 1894).
9. L. Barron, "Chirality and life," Space Sci. Rev. **135**(1-4), 187–201 (2008).
10. L. D. Barron, *Molecular Light Scattering and Optical Activity*, 2nd ed. (Cambridge University, 2009).
11. L. Nguyen, H. He, and C. Pham-Huy, "Chiral drugs: an overview," Int. J. Biomed. Sci. **2**, 85–100 (2006).
12. M. Schaeferling, D. Dregely, M. Hentschel, and H. Giessen, "Tailoring enhanced optical chirality: Design principles for chiral plasmonic nanostructures," Phys. Rev. X **2**(3), 031010 (2012).
13. V. Valev, J. Baumberg, C. Sibilia, and T. Verbiest, "Chirality and chiroptical effects in plasmonic nanostructures: Fundamentals, recent progress, and outlook," Adv. Mater. **25**(18), 2517–2534 (2013).
14. M. Nesterov, X. Yin, M. Schäferling, H. Giessen, and T. Weiss, "The role of plasmon-generated near fields for enhanced circular dichroism spectroscopy," ACS Photonics **3**(4), 578–583 (2016).
15. M. Schaeferling, *Chiral Nanophotonics - Chiral Optical Properties of Plasmonic Systems*, vol. 205 of *Springer Series in Optical Sciences* (Springer, 2017).

Optics EXPRESS

16. J. Collins, C. Kuppe, D. Hooper, C. Sibilia, M. Centini, and V. Valev, "Chirality and chiroptical effects in metal nanostructures: Fundamentals and current trends," Adv. Opt. Mater. **5**(16), 1700182 (2017).
17. X. Wang and Z. Tang, "Circular dichroism studies on plasmonic nanostructures," Small **13**(1), 1601115 (2017).
18. J. Mun, M. Kim, Y. Yang, T. Badloe, J. Ni, Y. Chen, C. Qiu, and J. Rho, "Electromagnetic chirality: from fundamentals to nontraditional chiroptical phenomena," Light: Sci. Appl. **9**(1), 139 (2020).
19. A. Lininger, G. Palermo, A. Guglielmelli, G. Nicoletta, M. Goel, M. Hinczewski, and G. Strangi, "Chirality in light–matter interaction," Adv. Mater. **34**, 2107325 (2022).
20. Y. Tang and A. Cohen, "Optical chirality and its interaction with matter," Phys. Rev. Lett. **104**(16), 163901 (2010).
21. Y. Tang and A. Cohen, "Enhanced enantioselectivity in excitation of chiral molecules by superchiral light," Science **332**(6027), 333–336 (2011).
22. M. Hentschel, M. Schäferling, X. Duan, H. Giessen, and N. Liu, "Chiral plasmonics," Sci. Adv. **3**(5), e1602735 (2017).
23. Y. Bai, Y. Li, M. Ikram, Y. Ren, Y. Xu, Y. Wang, Y. Huo, and Z. Zhang, "Circular dichroism induced by the coupling between surface plasmon polaritons and localized surface plasmon resonances in a double-layer complementary nanostructure," J. Phys. Chem. C **126**(24), 10159–10166 (2022).
24. J. Hu, Y. Xiao, L.-M. Zhou, X. Jiang, W. Qiu, W. Fei, Y. Chen, and Q. Zhan, "Ultra-narrow-band circular dichroism by surface lattice resonances in an asymmetric dimer-on-mirror metasurface," Opt. Express **30**(10), 16020–16030 (2022).
25. Z. Shen, S. Fan, W. Yin, S. Li, Y. Xu, L. Zhang, and X. Chen, "Chiral metasurfaces with maximum circular dichroism enabled by out-of-plane plasmonic system," Laser Photonics Rev. **16**(12), 2200370 (2022).
26. J. Kim, A. Rana, Y. Kim., I. Kim, T. Badloe, M. Zubair, M. Mehmood, and J. Rho, "Chiroptical metasurfaces: Principles, classification, and applications," Sensors **21**(13), 4381 (2021).
27. Y. Zhao, A. Askarpour, L. Sun, J. Shi, X. Li, and A. Alú, "Chirality detection of enantiomers using twisted optical metamaterials," Nat. Commun. **8**(1), 14180 (2017).
28. S. Yoo and Q.-H. Park, "Metamaterials and chiral sensing: a review of fundamentals and applications," Nanophotonics **8**(2), 249–261 (2019).
29. X.-T. Kong, L. Besteiro, Z. Wang, and A. Govorov, "Plasmonic chirality and circular dichroism in bioassembled and nonbiological systems: Theoretical background and recent progress," Adv. Mater. **32**(41), 1801790 (2020).
30. E. Petronijevic, A. Belardini, G. Leahu, T. Cesca, C. Scian, G. Mattei, and C. Sibilia, "Circular dichroism in low-cost plasmonics: 2d arrays of nanoholes in silver," Appl. Sci. **10**(4), 1316 (2020).
31. E. Petronijevic, H. Ali, N. Zaric, A. Belardini, G. Leahu, T. Cesca, G. Mattei, L. Andreani, and C. Sibilia, "Chiral effects in low–cost plasmonic arrays of elliptic nanoholes," Opt. Quantum Electron. **52**(3), 176 (2020).
32. B. Wu, M. Wang, P. Yu, F. Wu, and X. Wu, "Strong circular dichroism triggered by near-field perturbation," Opt. Mater. **118**, 111255 (2021).
33. E. Petronijevic, A. Belardini, G. Leahu, R. Voti, and C. Sibilia, "Nanostructured materials for circular dichroism and chirality at the nanoscale: towards unconventional characterization [invited," Opt. Mater. Express **12**(7), 2724–2746 (2022).
34. E. Petronijević, G. Leahu, R. Voti, A. Belardini, C. Scian, N. Michieli, T. Cesca, G. Mattei, and C. Sibilia, "Photo-acoustic detection of chirality in metal-polystyrene metasurfaces," Appl. Phys. Lett. **114**(5), 053101 (2019).
35. B. Maoz, A. Moshe, D. Vestler, O. B-Elli, and G. Markovich, "Chiroptical effects in planar achiral plasmonic oriented nanoholearrays," Nano Lett. **12**(5), 2357–2361 (2012).
36. K. McPeak, C. Engers, S. Bianchi, A. Rossinelli, L. Poulikakos, L. Bernard, S. Herrmann, D. Kim, S. Burger, M. Blome, S. Jayanti, and D. Norris, "Ultraviolet plasmonic chirality from colloidal aluminum nanoparticles exhibiting charge-selective protein detection," Adv. Mater. **27**(40), 6244–6250 (2015).
37. O. Arteaga, B. M. Maoz, S. Nichols, G. Markovich, and B. Kahr, "Complete polarimetry on the asymmetric transmission through subwavelength hole arrays," Opt. Express **22**(11), 13719–13732 (2014).
38. O. Arteaga, J. Sancho-Parramon, S. Nichols, B. M. Maoz, A. Canillas, S. Bosch, G. Markovich, and B. Kahr, "Relation between 2d/3d chirality and the appearance of chiroptical effects in real nanostructures," Opt. Express **24**(3), 2242–2252 (2016).
39. K. Dossou, L. Botten, A. Asatryan, B. Sturmberg, M. Byrne, C. Poulton, R. McPhedran, and C. Sterke, "Modal formulation for diffraction by absorbing photonic crystal slabs," J. Opt. Soc. Am. A **29**(5), 817–831 (2012).
40. B. Sturmberg, K. Dossou, F. P. R. McPhedran, C. Sterke, and L. Botten, "Emustack: An open source route to insightful electromagnetic computation via the bloch mode scattering matrix method," Comput. Phys. Commun. **202**, 276–286 (2016).
41. J. Rumble, ed., *CRC Handbook of Chemistry and Physics*, 103rd ed. (CRC, 2022).
42. R. Gordon, A. Brolo, A. McKinnon, A. Rajora, B. Leathem, and K. Kavanagh, "Strong polarization in the optical transmission through elliptical nanohole arrays," Phys. Rev. Lett. **92**(3), 037401 (2004).
43. J. Elliott, I. I. Smolyaninov, N. Zheludev, and A. V. Zayats, "Polarization control of optical transmission of a periodic array of elliptical nanoholes in a metal film," Opt. Lett. **29**(12), 1414 (2004).
44. K. Koerkamp, S. Enoch, F. Segerink, N. Hulst, and L. Kuipers, "Strong influence of hole shape on extraordinary transmission through periodic arrays of subwavelength holes," Phys. Rev. Lett. **92**(18), 183901 (2004).

Optics EXPRESS

45. K. van der Molen, K. Klein Koerkamp, S. Enoch, F. Segerink, N. Hulst, and L. Kuipers, "Role of shape and localized resonances in extraordinary transmission through periodic arrays of subwavelength holes: Experiment and theory," Phys. Rev. B **72**(4), 045421 (2005).
46. M. Schäferling, N. Engheta, H. Giessen, and T. Weiss, "Reducing the complexity: Enantioselective chiral near-fields by diagonal slit and mirror configuration," ACS Photonics **3**(6), 1076–1084 (2016).
47. G. Leahu, E. Petronijevic, R. Li Voti, A. Belardini, T. Cesca, G. Mattei, and C. Sibilia, "Diffracted beams from metasurfaces: High chiral detectivity by photothermal deflection technique," Adv. Opt. Mater. **9**(21), 2100670 (2021).
48. R. Li Voti, G. Leahu, E. Petronijevic, A. Belardini, T. Cesca, C. Scian, G. Mattei, and C. Sibilia, "Characterization of chirality in diffractive metasurfaces by photothermal deflection technique," Appl. Sci. **12**(3), 1109 (2022).
49. F. Graf, J. Feis, X. Garcia-Santiago, M. Wegener, C. Rockstuhl, and I. Fernandez-Corbaton, "Achiral, helicity preserving, and resonant structures for enhanced sensing of chiral molecules," ACS Photonics **6**(2), 482–491 (2019).
50. M. L. Solomon, J. Hu, M. Lawrence, A. García-Etxarri, and J. A. Dionne, "Enantiospecific optical enhancement of chiral sensing and separation with dielectric metasurfaces," ACS Photonics **6**(1), 43–49 (2019).
51. F. Mattioli, G. Mazzeo, G. Longhi, S. Abbate, G. Pellegrini, E. Mogni, M. Celebrano, M. Finazzi, L. Duó, C. G. Zanchi, M. Tommasini, M. Pea, S. Cibella, R. Polito, F. Sciortino, L. Baldassarre, A. Nucara, M. Ortolani, and P. Biagioni, "Plasmonic superchiral lattice resonances in the mid-infrared," ACS Photonics **7**(10), 2676–2681 (2020).